Spring 2019

Designing and 3D Printing mm-Wave Lenses Using Kel-F for Use in Dynamic Nuclear Polarization

Kellie McGuire
University of New Hampshire, Durham

Designing and 3D Printing mm-Wave Lenses Using Kel-F for Use in Dynamic Nuclear Polarization

Senior Thesis

Kellie J. McGuire
Advisor: Professor Elena Long

Department of Physics
University of New Hampshire
Durham, New Hampshire, USA
19 May 2019

Abstract

This thesis project presents a novel method of 3D printing with the fluoroplastic Kel-F (PCTFE) as an alternative to traditional machining and demonstrates its use in creating target cups for dynamic nuclear polarization (DNP) experiments. Kel-F is used by the UNH Nuclear Physics Group in its tensor-polarized target project because the material has several properties that make it well-suited to this purpose: transparency to millimeter-waves, plasticity at cryogenic temperatures, and the absence of any unpaired protons that would add an unwanted background to the NMR signal used to measure nucleon polarization. As this paper shows, these properties are not significantly altered by the printing process, validating the use of 3D-printed Kel-F components in a DNP system.

This paper also explores the possibility of using 3D printing to create mm-wave Kel-F lenses to be implemented into a DNP target system and presents the results of five such lenses using a 140 GHz Gaussian beam source and custom mm-wave imaging equipment. The results show that Kel-F lenses can be used to redistribute a mm-wave beam, but often at considerable power loss. These results highlight some of the design challenges to be overcome before such lenses will be effective at enhancing nucleon polarization.

Acknowledgments

I wish to express my deepest appreciation to Professor Elena Long for serving as my research advisor for almost two years. This thesis project demonstrates the scope of my work under Dr. Long's mentorship, and I am very proud of what I have been able to accomplish as her student.

In my time at UNH I have been the beneficiary of many talented and passionate educators. I wish specifically to thank Professors Maurik Holtrop, Benjamin Chandran, Elena Long, and Ningyu Liu for providing me with a strong physics foundation and for helping me foster a greater confidence in myself as an emerging physicist.

I am indebted to the researchers in Slifer Lab where I was able to participate in several DNP "cooldowns," of which this thesis project represents a small part. I especially wish to thank Nathaly Santiesteban, whose frequent drop-ins at Long Lab helped bridge the gap between our two labs and whose genuine interest in my research helped guide some of my decisions.

I am grateful to Mr. Dana Hamel and the UNH Hamel Center for Undergraduate Research for funding a portion of this project in an Undergraduate Research Award.

Finally, I wish to thank my husband, Ryan McGuire, for his unflagging words of encouragement during my years as a physics student at UNH and for regularly lending his expertise as a Python programmer to this project.

Contents

List of Figures

1 Introduction

The Nuclear Physics Group (NPG) at the University of New Hampshire is building a tensor-polarized solid deuterium target for nuclear physics experiments [1].

Tensor polarization is necessary to resolve observables that cannot be distingushed using a non-polarized or vector-polarized target [2][3]. The target being built by the NPG will be used in future experiments at Jefferson Lab to measure nucleon tensor observables, including the tensor asymmetry A_{zz} in the quasi-elastic region and the tensor structure function b_1 in the deep-inelastic region [4][1]. Measurements of A_{zz} will be used to describe the nature of the short-range nucleon repulsion and the tensor force strength, important for understanding short range correlations of nuclei. Measurements of b_1 will be used to probe exotic six-quark hidden color effects and quark orbital angular momentum.

The resolution of these experiments will depend, in part, on the degree of polarization of the target. To date, deuteron tensor-polarization of 15-20% has been achieved [5], and it is a central goal of the group to increase this to >30%, required for the A_{zz} and b_1 experiments.

This thesis project contributed to the NPG's tensor-polarized program in two main ways: (1) developed additive manufacturing techniques to help streamline the process of building the target system and (2) used these techniques to develop and test millimeter-wave lenses to be implemented into the target system to help enhance nucleon polarization.

2 Background and Motivation

Dynamic nuclear polarization (DNP) is a standard technique for creating a polarized nuclear target [6]. In DNP, the target is placed in a high magnetic field, cooled to cryogenic temperatures, and exposed to microwave radiation to induce spin transfer between unpaired electrons in the sample and the target nucleons. Nuclear magnetic resonance (NMR) techniques are used to measure the resulting polarization of the nucleons.

DNP is performed at temperatures approaching 1 K to drive up the thermal equilibrium polarization of the unpaired nucleons, as described by Maxwell-Boltzmann statistics [6]:

$$P_i = \tanh\left(\frac{g_i \mu_i B}{2 k_B T}\right). \tag{1}$$

Here g_i and μ_i are the g-factor and magnetic moment of a spin-1/2 particle, respectively, B is the magnitude of the applied magnetic field, T is the temperature of the system, and k_B is the Boltzmann constant. For a system in thermal equilibrium at 1 K in a 5 T magnetic field, $P_e \sim 99.8\%$ for electrons and $P_p \sim 0.12\%$ for protons. The large magnitude difference between the electron and proton polarization at thermal equilibrium is due to the proton's much smaller magnetic moment. In DNP, electron polarization is transferred to the target nucleons such that, in an ideal case, the maximum polarization of the target approaches that of P_e in thermal equilibrium.

To drive this polarization transfer, the target is irradiated at a frequency corresponding to the sum (negative polarization) or difference (positive polarization) of the spin resonance frequencies of the electron and target nucleon in the magnetic field,

$$\nu = B/2\pi \left(\gamma_e \pm \gamma_N\right), \tag{2}$$

where γ_e and γ_N are the gyromagnetic ratios of the electron and target nucleon/nucleus. In the case of protons in a 5 T field, $\nu \approx 140$ GHz, corresponding to a wavelength of ~2.14

mm ("mm-waves").

During DNP, the target is housed in small cups affixed to a target "ladder" and submerged in a superfluid helium cryostat (Fig 1). Because of the extreme conditions under which DNP is performed, a suitable material must be chosen for the target cups.

The fluoroplastic Kel-F (polychlorotrifluoroethylene [PCTFE]) has several properties that make it a favorable material for the DNP target cups: 1) it retains its plasticity at 1 K; 2) it is highly transparent to mm-wave radiation; and 3) it contains no hydrogen that would introduce a background into the NMR signal used to measure polarization. For these reasons, Kel-F has traditionally been used in DNP experiments [7]; however, the Kel-F components had to be machined.

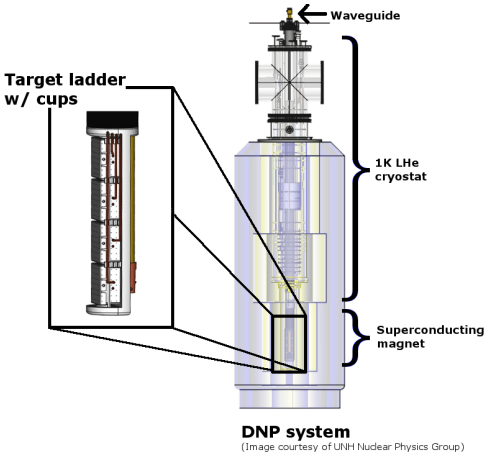

Figure 1: Dynamic nuclear polarization system. A target ladder with material cups, thermometry, and NMR circuit is placed at the center of a superconducting electromagnet in a cryostat.

With recent developments in 3D printing, as outlined in this paper, the Nuclear Physics Group at UNH can now 3D-print the Kel-F target cups. 3D printing offers several advantages over machining, including rapid prototyping and the ability to manufacture parts with complex geometries and fine details that would be difficult or impossible to machine. One application of this is the development of 3D-printed Kel-F mm-wave lenses to be implemented into the DNP target cups. Such lenses could be used to evenly distribute the incident mm-wave beam and uniformly saturate the target, thus driving up the degree of nucleon polarization.

3 3D Printing with Kel-F

Additive manufacturing (i.e., 3D printing) is a rapidly expanding technology that has found its way into physics laboratories looking to benefit from the ability to manufacture custom parts quickly and at low cost [8][9]. Several different 3D-printing methods exist. A common method of 3D printing, known as fused filament fabrication, extrudes molten filament through a nozzle, depositing it onto a print bed and building the model layer by layer. New 3D-printing techniques and materials appear on the market regularly. At the writing of this paper, however, there are few resources available for 3D printing with fluoroplastics, and none for Kel-F.

A major focus of this work has thus been to develop a method of 3D printing with Kel-F, including manufacturing the printable filament. Fluoroplastics pose several challenges, described in the following sections, over conventional 3D-printing materials, such as polylactic acid (PLA) and acrylonitrile butadiene styrene (ABS). In anticipation of these challenges, early work was performed using fluorinated ethylene propylene (FEP), a fluoroplastic similar to Kel-F but with a larger temperature window in which it can be processed. Printing with FEP, however, proved more challenging than with Kel-F, and work with FEP was halted once Kel-F filament production was underway.

3.1 Safety Concerns

Kel-F and FEP are fluoropolymers (Fig. 2), and special care must be taken when processing the material, as the molecules will begin to degrade and release chlorine and/or fluorine gases upon reaching their melting point [10]. This is especially the case for Kel-F, which is less thermally stable than FEP due to its lower fluorine content [11].

To minimize the risk of contamination, all fluoroplastic processing is performed in a fume hood. Any heated brass or copper components (nozzles) must be replaced with stainless steel or aluminum, or be nickel-coated, as the copper acts as a catalyst for the decomposition into hydrofluoric acid (HF) and hydrochloric acid (HCl) [12].

Prior to filament production, the UNH Office of Environmental Health and Safety (OEHS) performed air and surface contamination tests on FEP and Kel-F heated to 310° C and 380° C, respectively. All tests yielded values below the EPA limits of 4 mg/L for fluoride and 250 mg/L for chloride recommended in drinking water [13].

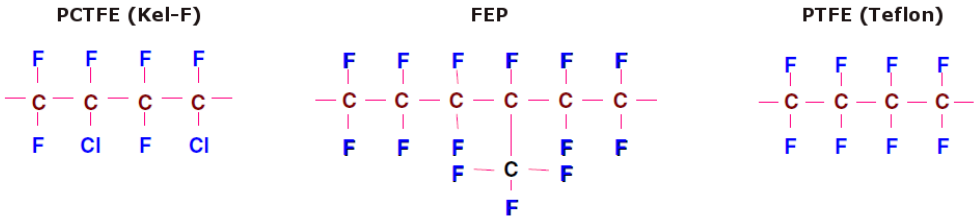

Figure 2: Fluoroplastic molecules, obtained from [14]. The higher fluorine content of FEP and PTFE (Teflon) makes the molecules more thermally stable than Kel-F, which degrades quickly upon melting.

3.2 Filament Production

One of the challenges of working with Kel-F is finding the optimal temperature and speed at which to melt and extrude the material. Kel-F is a semi-crystalline polymer, and its degree of crystalinity can vary considerably and increases with prolonged heat exposure [10]. The higher the crystalinity of Kel-F, the more glassy and brittle it becomes [15], so it is necessary to melt, extrude, and cool the material as quickly as possible to minimize crystallization. Because Kel-F has a high melt viscosity [10], it must be processed at a temperature well above its melting point. However, as noted above, Kel-F is also thermally unstable and will decompose rapidly at high temperatures. Hence there is a small temperature and time window in which Kel-F can be processed without significantly altering its desired properties.

In contrast, FEP is more thermally stable than Kel-F due to its increased fluorine content [11], but otherwise shares many of the properties of Kel-F, such as high processing temperature and high melt viscosity. Filament making processes were thus first developed for FEP, with the intention of applying the same methods to Kel-F production once refined. However, as discussed below, this process did not transfer over well to Kel-F, and a different method had to be sought.

3.2.1 FEP Filament

To produce FEP filament, a commercially available device (the "Filastruder" [16]) was used, which consists of a screw and barrel that delivers the material in pellet form to a hot end where it is melted and extruded through a die. The default stainless steel hot end and brass die were replaced with aluminum to reduce the temperature gradient and prevent catalytic decomposition. The FEP pellets were made in-house using a custom device, the "Pelletizer," which chops the bulk material into uniform pellets.[1]

Early efforts to produce FEP filament resulted in brown, ropey filament that was entirely unsuitable for 3D printing. This was likely due to having processed the material at too low a temperature for extrusion and overexposing the material to heat as it slowly melted. The melting point of FEP is approximately 260°C, but as with all fluoroplastics, FEP has a high melt viscosity [11] and must be processed at temperatures well above its melting point before it will extrude through small diameters. The best results were obtained by heating the FEP to 380°C and extruding at a rate of approximately 60 cm/min through a diameter of 1.75 mm, desirable for 3D-printer filament. Even at these settings, the FEP filament retained a slight brown tint (Fig. 5).

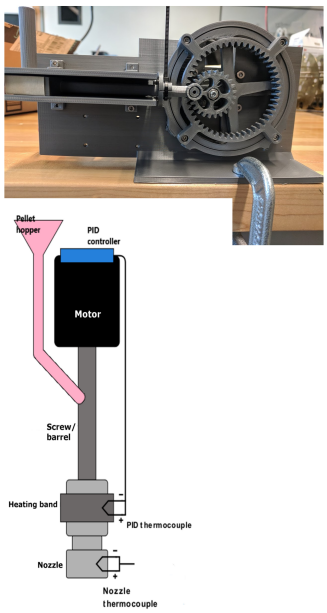

Figure 3: System used to create FEP filament, featuring the Pelletizer (top) and Filastruder (bottom).

3.2.2 Kel-F Filament and "Filatizer"

Kel-F is a much harder material than FEP, with a Shore D hardness of approximately 90, versus 56 for FEP [15][18]. Because of this, the Pelletizer was ill-suited to chopping the bulk Kel-F into pellets. Further, the Filastruder screw had difficulty turning under the load of the unmelted pellets, causing the motor to stall. Without a viable commercial option for obtaining smaller-size pellets, an alternative method of making Kel-F filament was necessary.

A new device was developed, the "Filatizer" (Fig. 4), which melts the bulk material directly, bypassing the need to chop the material into pellets. This design has the added benefit of significantly reducing the volume of material in the hot end, which increases the processing speed of the material and results in cleaner filament with less crystallization (Fig. 5).

Because of Kel-F's high melt viscosity, the speed and temperature at which high-quality filament can be extruded is largely dependent on the diameter of the die. Good results were obtained at several different settings, as given in Table 2 in Appendix A.

[1] All fluoroplastic filament production began with raw material in the form of long, 0.187-inch diameter rods obtained from Professional Plastics, Inc. [17].

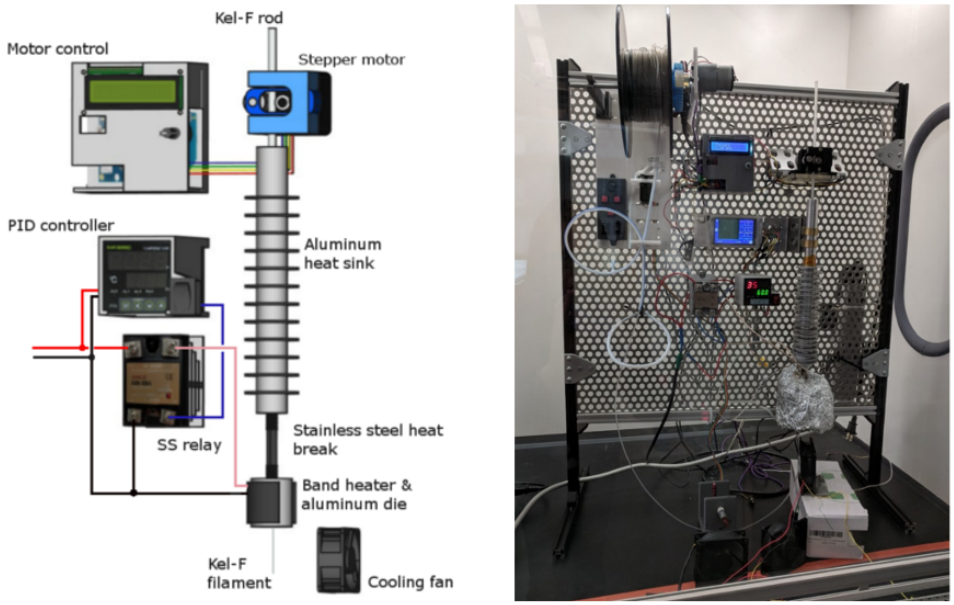

Figure 4: "Filatizer" filament production system. An alternative to the screw and barrel assembly, the Filatizer uses a stepper motor to feed the bulk material directly into a hot end, where it is extruded through an aluminum die. A fan cools the extruded filament to reduce crystallization.

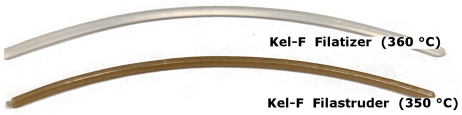

Figure 5: Fluoroplastic filament produced using the Filastruder and Filatizer. The best results were obtained with the Filatizer, which has a much smaller hot end than the Filastruder, reducing the material's exposure to heat.

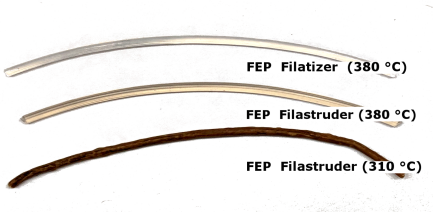

3.3 Kel-F Printing

All Kel-F printing was performed using a modified Prusa i3 MK2.5S printer [19]. To accommodate temperatures above 300°C, the aluminum heater block was replaced with nickel-coated copper [20], and the printer was modified to use a Type K thermocouple in place of the thermistor at the hot end. To prevent catalytic decomposition, the default brass nozzle was replaced with hardened steel.

Kel-F, like other fluoroplastics, is a slippery material with a low coefficient of static friction [11]. One of the major challenges of printing with the material is getting the component to adhere to the printer bed and remain affixed for the duration of the print. Kel-F will not adhere directly to the printer bed, at least not at bed temperatures below 120°C, the limit of the Prusa printer. The material might adhere better at a bed temperature closer to the melting point of Kel-F (212°C); however, such high temperatures would dramatically slow the cooling of the print, and this would likely result in the material losing its plasticity as it cooled. Instead, Kel-F can be printed atop a layer of high-temperature silicon glue on adhesive transfer tape [21], which can be easily applied to the print bed. This works quite well but leaves a residue on the bottom of the print that must be cleaned in post-processing.

The problem of bed adhesion is compounded by the tendency of the material to curl up and off of the printer bed during the print. The effect is most pronounced at sharp corners, likely due to the material contracting as it cools. The effect can be reduced by designing the component to have thin circular "feet" at the corners, which helps to slow the cooling of the material at the edges and can be cut away once the print is complete (Fig. 6). This method works better than printing the model with a brim or raft,[2] which do nothing to stop the print from curling off the bed.

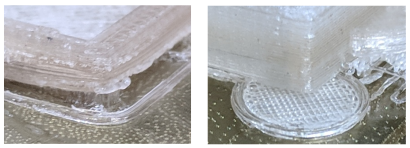

Figure 6: Kel-F printer bed adhesion is improved by adding circular "feet" to sharp edges.

Fine-tuning the print settings is imperative for a successful Kel-F print. While true of fused filament fabrication in general, this is especially true when printing with Kel-F, as even slight variations in print speed and temperature can dramatically affect the quality of a print (Fig. 7). Table 3 in Appendix A lists several print settings that have resulted in successful prints.

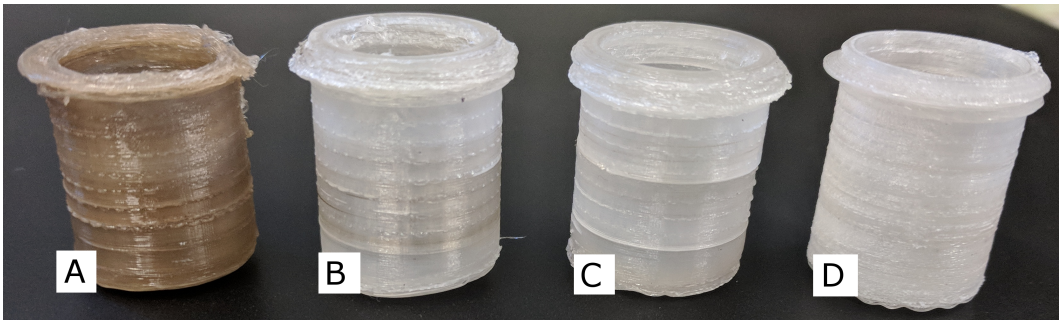

Figure 7: 3D-printed Kel-F DNP target cups. (A) was printed with filament from the Filastruder; (B) and (C) were printed with filament from the Filatizer and show considerable color improvement but contain regions that are glassy and brittle (visible as distinct lines); (D) was printed at a faster extrusion speed and the material retained its plasticity.

[2] A typical way of improving bed adhesion is to print the part with a brim or raft, described at https://www.simplify3d.com/support/articles/rafts-skirts-and-brims/.

4 Lens Design and Testing

4.1 Equipment

4.1.1 Millimeter-Wave Source

At the heart of the NPG's tensor-polarized target project is a 5 T superconducting magnet, which supplies sufficient field strength to polarize >99% of the target material's unpaired electrons at 1 K (Eq. 1). To induce electron-to-nucleon spin transfer at this field strength, a millimeter-wave (mm-wave) source of 140±2 GHz ($\lambda \approx 2$ mm) is used.

The source of the mm-wave radiation is a DNP/EPR system custom-manufactured by Bridge12 Technologies. The radiation is generated from a built-in LabBrick synthesizer (model LMS-123), which generates an 11.5-11.83 GHz adjustable signal. The signal is up-converted to 140±2 GHz using a high-frequency, solid-state amplification-multiplication chain (VDI 12x AMC 657). The beam is directed through a series of quasi-optical mirrors that refocus and circularly polarize the beam. The resulting signal is a 0-450 mW Gaussian beam whose power can be adjusted by setting the voltage on an attenuator. An external circular waveguide (length 191 cm; inner diameter 14.5 mm) is used to direct the beam to the DNP target.

The Gaussian beam (Fig. 8) is characterized by its wavelength, λ, and beam waist, w_0, the radius of the beam at its narrowest point, which measures 4.085 mm for the DNP/EPR system [22]. From these parameters, the beam size at a distance z from the beam waist can be calculated using the relations [23]

$$z_R = \frac{\pi \omega_0^2}{\lambda}, \tag{3}$$

$$\omega^2(z) = \omega_0^2 \left(1 + \frac{z^2}{z_R^2}\right). \tag{4}$$

Here z_R is the Rayleigh range, the distance from the beam waist where the beam size has grown by a factor of $\sqrt{2}$, and ω is the beam spot size, which corresponds to the transverse distance from the beam axis at which the irradiance has fallen to e^{-2} its on-axis value. The irradiance of the beam can be obtained from

$$I(\rho, z) = I_0 \left(\frac{\omega_0}{\omega(z)}\right)^2 e^{-2\rho^2/\omega^2(z)}, \tag{5}$$

where I_0 is the maximum irradiance, measured at the center of the beam waist, and ρ is the transverse distance from the beam axis.

4.1.2 Beam Irradiance Measurements and Calorimeter

For Kel-F lens design and testing, the beam was imaged using custom-made mm-wave absorbers that were 3D-printed with iron-infused PLA. The iron was chosen to enhance the efficiency of the material at absorbing the mm-waves [24], although this property was not directly tested. The relative intensity of the beam and its irradiance profile are depicted in the temperature gradient of the absorber in the beam path.

Temperature-sensitive liquid crystal sheets attached to the absorber can be used to observe the temperature gradient; however, this method has many limitations. For one, such observations are highly subjective and cannot resolve small temperature differences

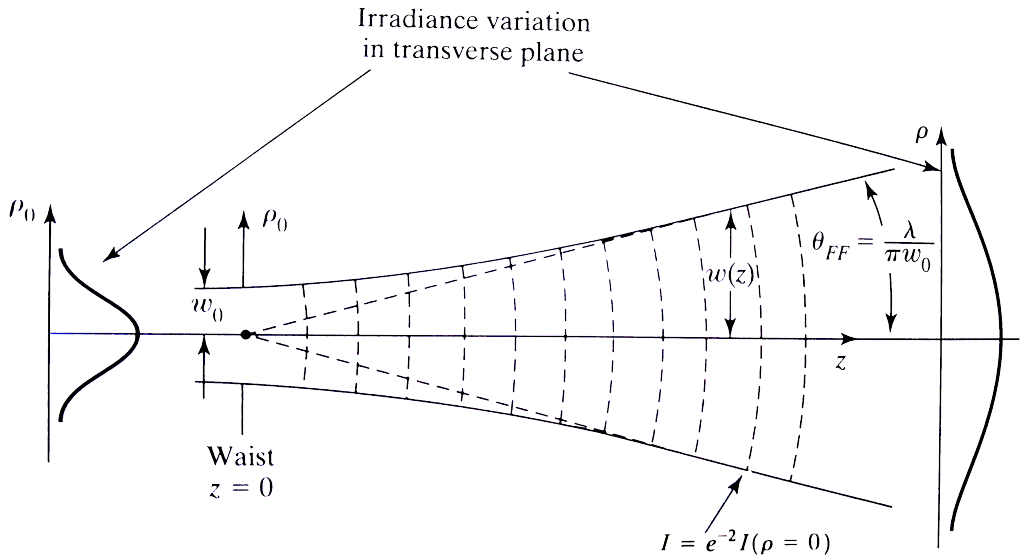

Figure 8: Gaussian beam characterized by its wavelength, λ, and beam waist, ω_0. Modified from [23].

(<0.1°C). Further, the liquid crystal sheets are slightly heat conductive and will form a narrow gradient band unrelated to beam irradiance. The liquid crystal sheets are most useful for getting a quick, qualitative sense of the beam's size and intensity at various locations along its path.

For detailed data on beam profile and power loss through Kel-F, a custom calorimeter was used. The sensor consists of an array of 25 thermally isolated "pixels," each containing a precision thermistor (Littelfuse PR103J2). The sensor was controlled using a multiplexer circuit driven by an Arduino Nano with external ADC for 11-bit resolution. The sensor measures temperature differences of 0.05 ±0.07°C. This level of precision is necessary to resolve the Gaussian profile of the mm-wave beam and to measure power loss as the beam passes through different Kel-F components. Data from the sensor were used to generate a heat map that characterized the irradiance profile of the beam (Fig. 9).

Although designed to capture the beam profile, the sensor can also measure the power output of the mm-wave source up to 200 mW, where it begins to saturate (Fig. 10). The power output curve was calculated by noting the temperature difference of the center pixel over a 20-second window in which the heating was linear and using the specific heat of the sensor material (iron-infused PLA), along with the density and volume of the pixel, to calculate the power on the sensor.

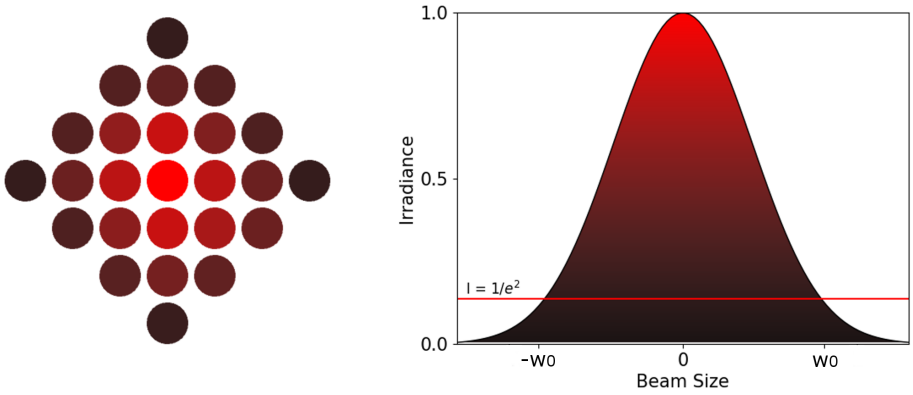

Figure 9: Irradiance of unobstructed beam on sensor placed 10 cm from waveguide mirror (left) features a Gaussian profile (right).

Figure 10: Millimeter-wave power output versus voltage on attenuator. The VDI curve is the actual power from the mm-wave system. The Bridge12 data was taken using a power meter that began to saturate around 250 mW. The calorimeter data was measured at the beam waist, and the sensor begins to saturate around 200 mW.

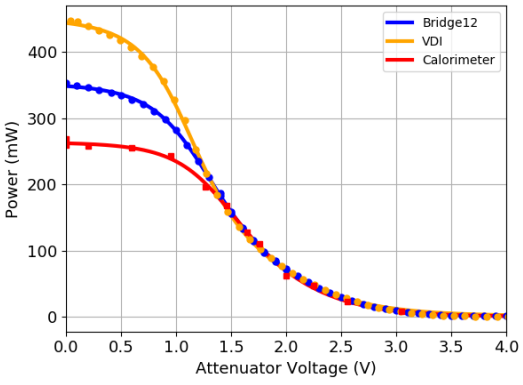

4.1.3 Temperature-Controlled Box

From Eq. 4, the maximum beam irradiance drops by approximately 70% in the waveguide (ω = 7.25 mm). Further beam spread occurs in the distance between the end of the waveguide and the DNP target. For a target placed 1 cm from the center of the waveguide mirror (a typical distance for the DNP target system), the beam will have propagated an effective distance of $z \approx 6.2$ cm, corresponding to a peak irradiance of only 14% the value at the waist. This increases the difficulty of imaging the beam using mm-wave absorbers, as the total power (450 mW maximum) is now spread over an area 7 times the size of the beam at the waist. For the purposes of imaging the beam through Kel-F lenses, the sensor must be placed even farther from the waveguide mirror, resulting in a temperature gradient of 1-2°C across the beam profile, as measured by the sensor. A carefully controlled environment is therefore desirable for making beam measurements using the calorimeter.

To reduce ambient temperature fluctuations that could corrupt the image of the beam, a temperature-controlled box was devised (Fig. 11). The box was kept several degrees above room temperature (e.g., 35±(0.3)°C) using a 12 V, 1.2 Ω heat bed (Prusa MK42) repurposed from a Prusa i3 MK2 3D printer. The bed was PID-controlled at 5 V, which underpowers the bed to minimize the temperature cycle of the box (approx. 4 minutes). The heating from the bed produces a small temperature gradient (0.4°C) across the sensor pixels, which can be subtracted out after data acquisition. Temperature cycling on the pixels themselves ranges from 0.05°C to 0.15°C over one box cycle and can be averaged over to get the total heating from the beam alone.

The box was insulated on 5 of its 6 faces using foam insulation and aluminum foil for thermal deflection. Circulation fans helped to regulate the temperature inside the box and speed up the cooling of the sensor pixels after each measurement.

The box supplies the necessary environment for using liquid crystal sheets to image the beam, as the only commercially available sheets with better than 1°C resolution operate in the range of 35-36°C [25]. For measurements using the calorimeter, the box provides a consistent, controlled environment that allows for direct comparison of data gathered over many days, as initial temperature conditions are easy to reproduce and long-term conditions easy to control.

4.2 Dielectric Properties of Kel-F

For designing lenses and other 3D-printed Kel-F components for DNP applications, a detailed study of the dielectric properties of the material at 140 GHz is desirable. A thorough study would make use of a vector network analyzer (VNA) or similar instrument to measure the complex permittivity of the 3D-printed Kel-F components at the desired frequency. The resulting data could be used to calculate the refractive index, reflection, and power loss through the material, properties that might be altered by the 3D-printing process. Modern vector network analyzers in the microwave range, however, are quite expensive and not available for this work. High-end VNAs max out in the tens of GHz range and must be paired with external frequency extenders to boost the output signal into the mm-wave range.

For the purposes of designing Kel-F components, lower-frequency measurements do not suffice for predicting how the material will perform at 140 GHz. Due to Kel-F's chlorine content, the material has a permanent dipole moment [11]. This makes the complex permittivity highly frequency-dependent, at least up to the cutoff frequency for dipole rotation, usually in the microwave region [26]. This is in contrast to the fluoroplastics FEP and PTFE (Teflon), whose permittivity is largely constant over a wide frequency range [11].

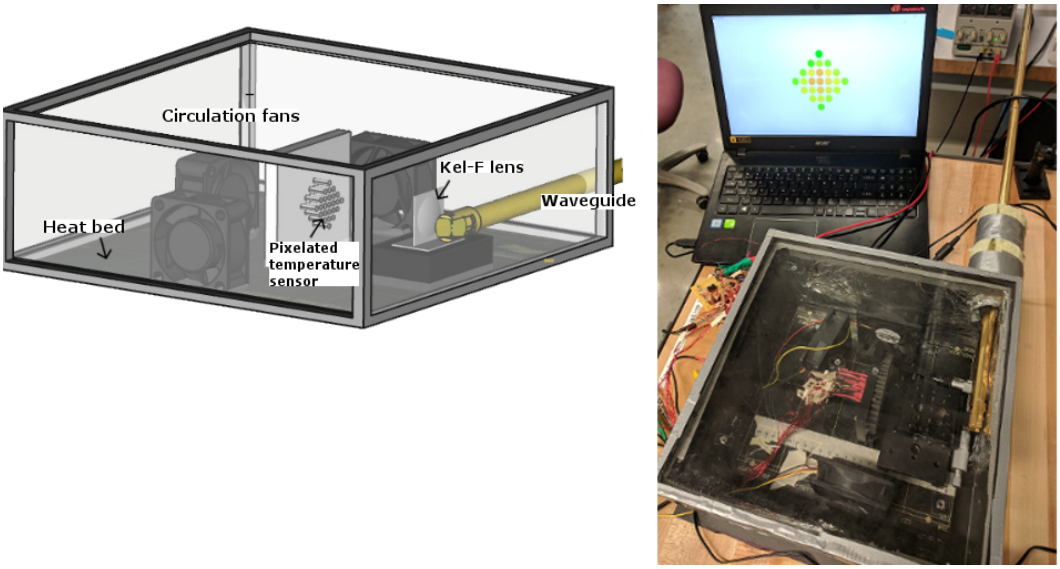

Figure 11: An insulated and heated box provided a controlled environment for imaging the mm-wave beam at the far end of the waveguide, where the irradiance has dropped to less than a third its value at the beam waist.

In lieu of thorough dielectric measurements, the refractive index of 3D-printed Kel-F at 140 GHz was estimated by sending the mm-wave beam through a 3D-printed prism and noting the angle of minimum deviation, δ_{min} (Fig. 12). The refractive index was then calculated using the relation

$$n = \frac{\sin\left(\frac{A+\delta_{min}}{2}\right)}{\sin\left(\frac{A}{2}\right)}, \tag{6}$$

where A is 60° for the prisms.

This process uncovered a significant inconsistency (n measured between 1.46 and 1.51) obtained using prisms of varying print quality. This can be understood in part from the results of A.H. Scott, et al. [27], which show that the degree of crystallinity of Kel-F plays a role in its permittivity (Fig. 13).

The study also highlights the temperature-dependence of Kel-F's dielectric properties. Unlike PTFE, whose permittivity is remarkably consistent over a large temperature range [14], Kel-F, differing from PTFE in a chlorine atom (Fig. 2), has a large temperature-dependence. This highlights the limitations of designing and testing Kel-F lenses at room temperature that are meant for cryogenic application. This temperature dependence, however, largely drops out beyond the cutoff frequency of dipole rotation and can be expected to play a lesser role in the mm-wave range. On the other hand, as the A.H. Scott study shows, a higher-frequency loss mechanism arises in Kel-F samples with a large degree of crystallinity, which the authors attribute to a bulk property of the crystal. These results underscore the importance of minimizing the crystallinity of the Kel-F components.

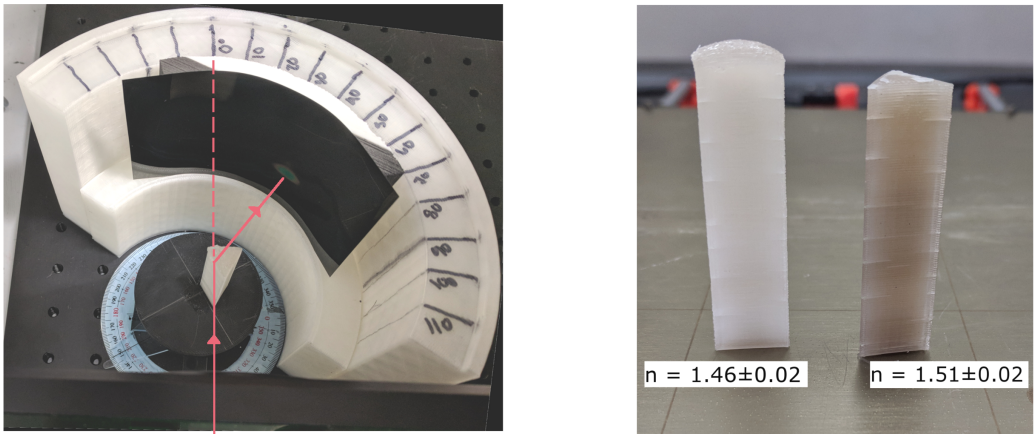

Figure 12: The angle of deviation of a refracted mm-wave beam through Kel-F was imaged using a 3D-printed absorber and temperature-sensitive liquid crystal sheet. The refractive index of 3D-printed Kel-F is highly dependent on the quality of the print.

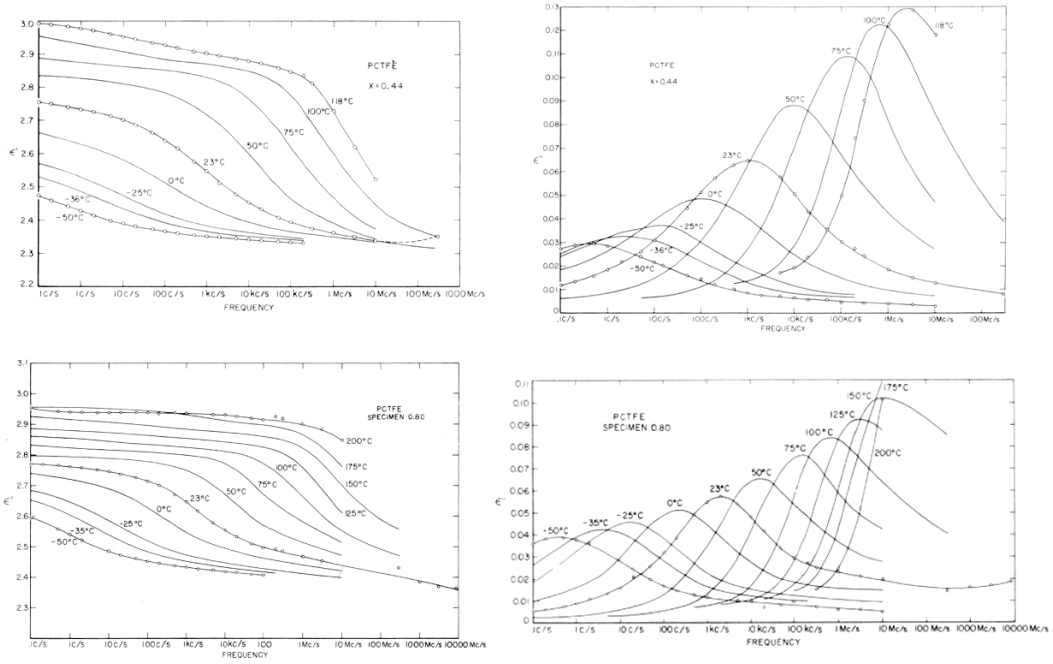

Figure 13: Plots of the frequency (logarithmic scale from 1 Hz to 1GHz) and temperature dependence of real (ϵ') and imaginary (ϵ'') permittivity of Kel-F (PCTFE) with 44% (top) and 80% (bottom) crystallinity. Obtained from [27]. The authors attribute the high-frequency tail in the bottom-right plot to a bulk polarization of the crystals in the material.

4.3 Lens Design

Developing a focusing lens provides a means of testing the refractive index of the 3D-printed Kel-F and evaluating its overall optical behavior. This is a good place to start, as the performance of a focusing lens is, at least in principle, easy to evaluate – it should merely re-create the beam waist at the focal plane.

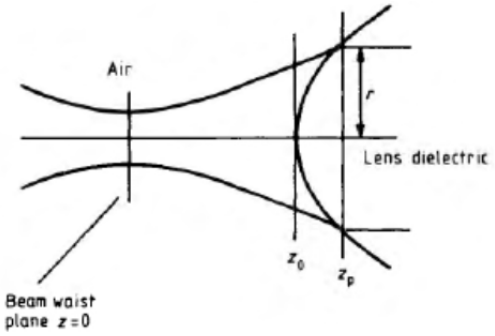

Figure 14: A hyperbolic lens designed to produce a plane wave. Obtained from [29].

Diffraction effects, however, become important when designing a lens to focus mm-waves in the near field [28]. One way to reduce diffraction losses is to design the lens with a diameter at least three times the beam waist at the incident plane [29], although this has the undesired consequence of increasing lens thickness and thus absorption (described in detail in Sect. 6.2). One can also design a lens face that takes into account the phase of the beam at different points on the lens surface. The equations for such a lens are given in Appendix A and were the inspiration for the design of the focusing lens featured in this study. A lens of this design effectively creates a plane wave inside the lens (Fig. 14) and simplifies the design of the second lens face, which need no longer account for the curvature of the beam. However, this design can increase the thickness of the lens and is worth pursuing only if the lens material is highly transparent to the beam, as absorption losses can outweigh diffraction losses.

5 Results and Discussion

5.1 Target Cup Performance

The 3D-printed Kel-F cups underwent cryogenic temperature cycling and impact testing prior to their use in the DNP system. The test cups were attached to a target ladder 3D printed with Formlabs Durable resin. The ladder was submerged in 77 K liquid nitrogen and subsequently heated using a hot air blower. This was performed six times, with no visible damage or microfractures on the cups. For impact testing, the target ladder was submerged in liquid nitrogen and then dropped from increasing heights onto the laboratory floor. All but one of the cups remained intact. The results of the tests are given in Table 1.

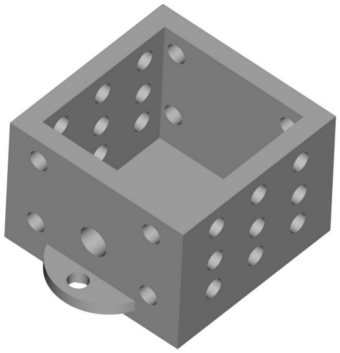

Figure 15: DNP target cup.

Table 1: Temperature cycling from 77 K to 300 K and impact test results for 3D-printed Kel-F cups. Cups 1 and 2 were attached to a target ladder, printed using Formlabs Durable resin, using superglue; cups 3 and 4 were attached using DP190 epoxy.

Cup No.	Temp. cycling results	Drop test results
1	Intact after 6 cycles	Cup intact after drop of 35 in.; detached from ladder
2	Intact after 6 cycles	Cup intact after drop of 35 in.; detached from ladder
3	Intact after 6 cycles	Break along layer with helium holes at drop of 8 in.
4	Intact after 6 cycles	Cup intact after drop of 4 ft; ladder shattered

Figure 16: DNP target ladder printed using Formlabs Durable resin with NMR coils and rectangular 3D-printed Kel-F cups after cooling to 1 K. The cup on the far left was removed to allow access to the NMR circuit.

5.2 Millimeter-Wave Loss Through Kel-F

As discussed in the Background and Motivation section, Kel-F is used for DNP target cups in part because it is highly transparent to mm-waves. It is important to determine whether this holds true for 3D-printed Kel-F components if they are to replace solid, machined components in DNP experiments.

Absorption measurements were performed with the calorimeter positioned 10 cm from the waveguide mirror in the temperature-controlled box. For each measurement, a different Kel-F component of known thickness was positioned at the beam waist, blocking the entrance to the waveguide. The beam was activated with 0.50 ± 0.01 V on the attenuator, corresponding to a power output of approximately 420 mW. For each measurement, the beam remained on for 16 minutes to allow the center (hottest) pixel to reach saturation and for the box to complete one full heating and cooling cycle with the pixel saturated. The beam was then deactivated and the calorimeter allowed to cool and reach thermal equilibrium with the box before the next measurement was performed. The total heating of the pixel was calculated by taking the average temperature over a full box cycle after saturation and subtracting off the initial temperature of the pixel. Results are presented in Fig. 17.

A comparison of the slopes of the two Kel-F fits suggests that 3D-printed Kel-F might be slightly less transparent than solid Kel-F, although more data would be necessarily to confirm this. The relatively steep slopes of both Kel-F fits, however, indicate that the

material is less transparent to 140 GHz radiation than anticipated, although still more transparent than Formlabs Durable resin, which was used to print the target ladder in Fig. 16 and was used for previous versions of the target cups while the Kel-F printing method was being developed.

The discontinuity of the data at a thickness of zero (unobstructed beam) is an indication of surface reflection. The fact that the data do not precisely overlap for the unobstructed beam is less a result of error in the measurements and more a result of having to reposition the waveguide, which had a tendency to get misaligned and is in large part why more measurements weren't included in the analysis.

A close inspection of the discontinuity suggests that 3D-printed Kel-F might be experiencing more surface reflection than solid Kel-F, although more data will be necessary to confirm this. If this is confirmed, surface reflection can likely be reduced by sanding or polishing the surfaces to make them smoother.

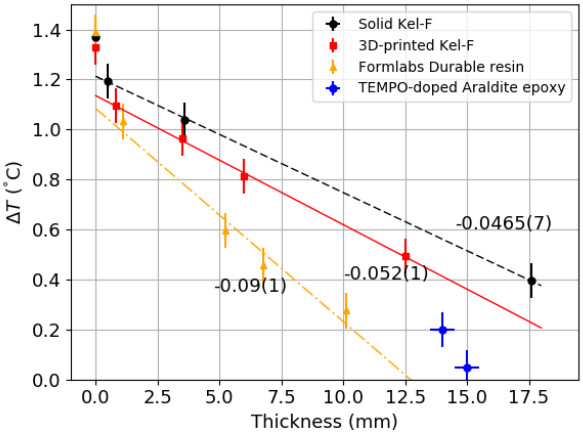

Figure 17: 140 GHz loss through Kel-F and other materials. The steep slopes of the two Kel-F fits (presented with their standard errors) indicate that the material is less transparent than expected, while still more transparent than Formabs Durable resin. The discontinuities at a thickness of zero indicate surface reflection. Also shown is the mm-wave loss through a TEMPO-doped epoxy target, for which absorption is desired.

5.3 Lens Performance

Five 3D-printed lenses were evaluated in this study. The dimensions of the lenses are given in Appendix B.

All measurements were performed with the lens positioned 1 cm from the center of the waveguide mirror and the sensor positioned 7.5 cm from the lens, except where noted. To avoid inconsistency across measurements due to the heating from the box itself, the beam was turned on at the same moment in the box cycle (the point at which the PID controller triggered). For each measurement, the beam was set to maximum power (450 mW), and the sensor pixels were heated for the duration of a half-cycle of the temperature-controlled box ($\approx$ 115 seconds), corresponding to a time at which the coolest pixels would have already reached saturation. Between tests, the sensor pixels were allowed to cool until they reached thermal equilibrium with the temperature box. The total heating of each pixel was calculated by taking the average over the last 33 seconds of the data run (200 values) and subtracting the average of the first 10 values before the beam was activated.

In light of the results presented in Sect. 6.2, some loss due to surface reflection and absorption is to be expected for the lenses. Lens performance was thus evaluated by comparing the beam transmittance through the lenses with that of a flat 3D-printed Kel-F disk

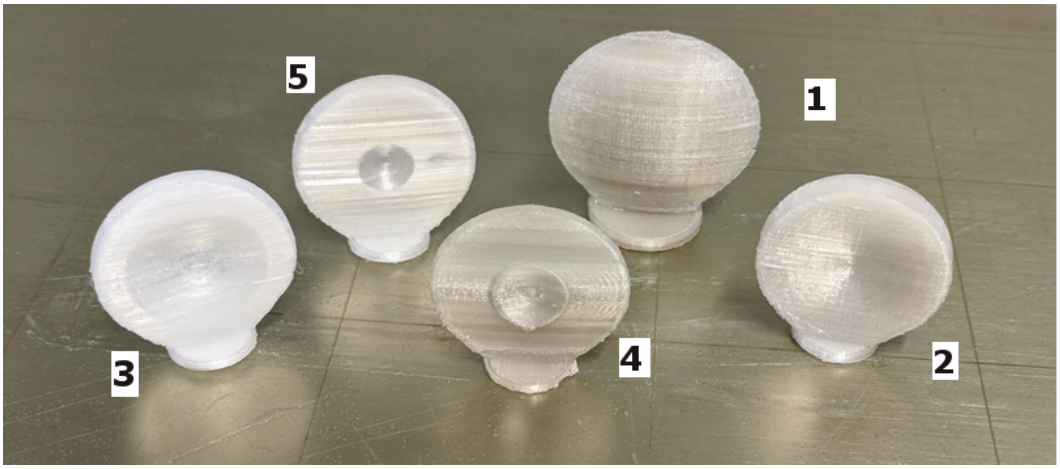

Figure 18: 3D-printed Kel-F lenses.

with a thickness of 2.5 mm, corresponding to the approximate thickness of a Kel-F target cup wall.

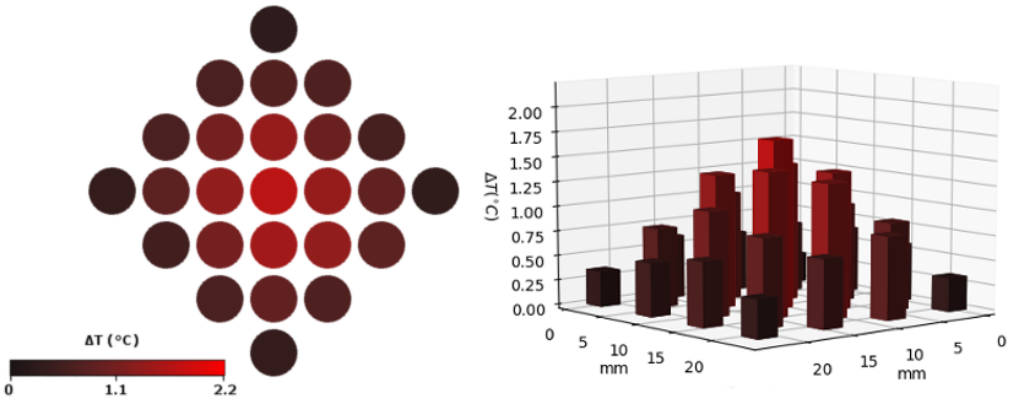

Figure 19: Beam transmittance through 2.5-mm 3D-printed Kel-F disk with sensor positioned 7.5 cm from the disk.

5.3.1 Lens 1 (Focusing Lens)

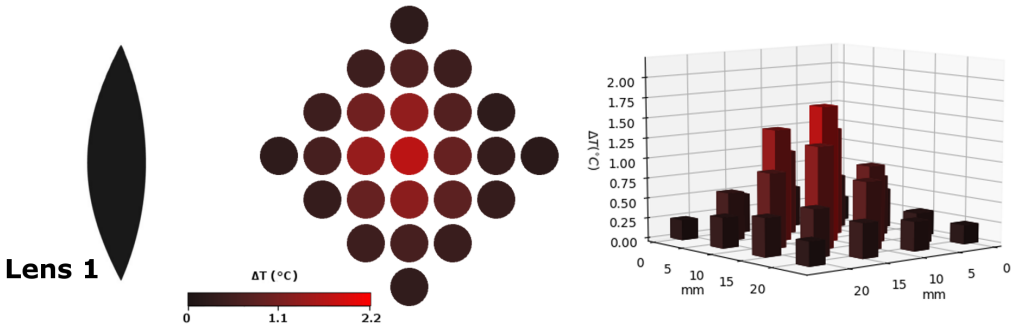

Figure 20: Results for Lens 1, with the sensor positioned 7.5 cm from the lens.

Lens 1 is a focusing lens designed to recreate the beam waist at the focal plane. A focused beam will appear as one or two bright pixels at the center of the sensor array, with minimal heating elsewhere. The results show that the sensor, positioned 7.5 cm from the lens, is not located at the focal plane but that the lens is nevertheless focusing. This can be seen most clearly in Fig. 21, where the values of the center row of sensor pixels are plotted. At 7.5 cm from the lens, the maximum irradiance through the lens is comparable to that through the 2.5-mm disk at a point where the lens is 4 times thicker than the disk (i.e., along the center of the beam). A second measurement with the sensor placed 4 cm from the lens shows a more-focused beam, indicating that the focal plane is within 7.5 cm of the lens.

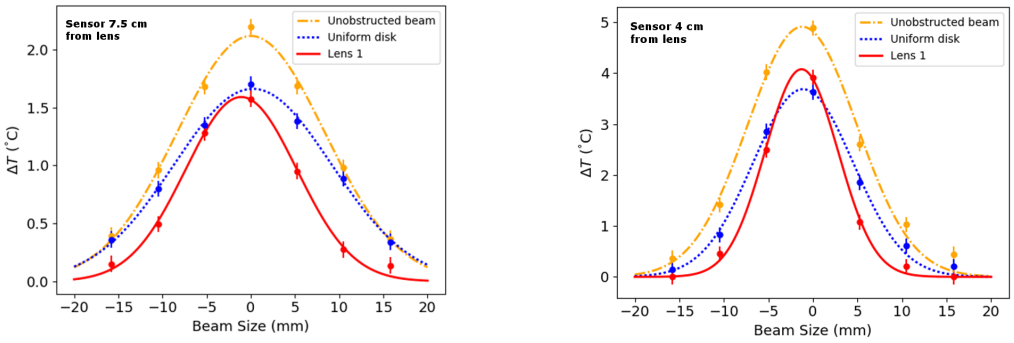

Figure 21: A comparison of the beam profile through Lens 1 (focusing lens) with the sensor at two different locations indicates that the focal plane is within 7.5 cm of the lens.

5.3.2 Lens 2 (Inverted Lens)

This lens was designed by inverting Lens 1 to diverge the center "hot spot" of the beam. The results show significant mm-wave loss at the location of the sensor. Further analysis is necessary to determine whether the beam has diverged beyond the solid angle of the sensor or whether the loss is consistent across the full beam profile.

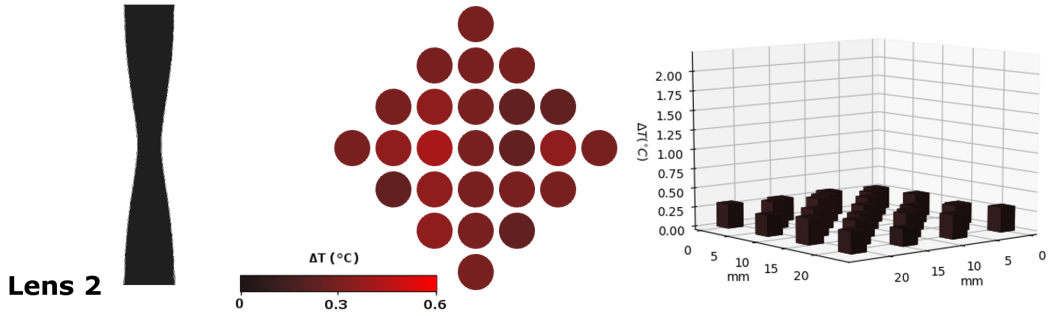

Figure 22: Results for Lens 2, with the sensor positioned 7.5 cm from the lens, show significant power loss at the location of the sensor. Note the small temperature range of the center image.

This lens suffers from several design flaws that are likely causing additional loss through the lens. For one, the curvature along the incident plane of the lens is likely increasing surface reflection. Also, the lens material is thicker at a radius where the incident beam is less intense, contributing to greater absorption losses there. Another concern is that the lens is introducing diffraction losses due to the non-uniform angle through which the beam is being diverged.

5.3.3 Lens 3 (Conic Lens)

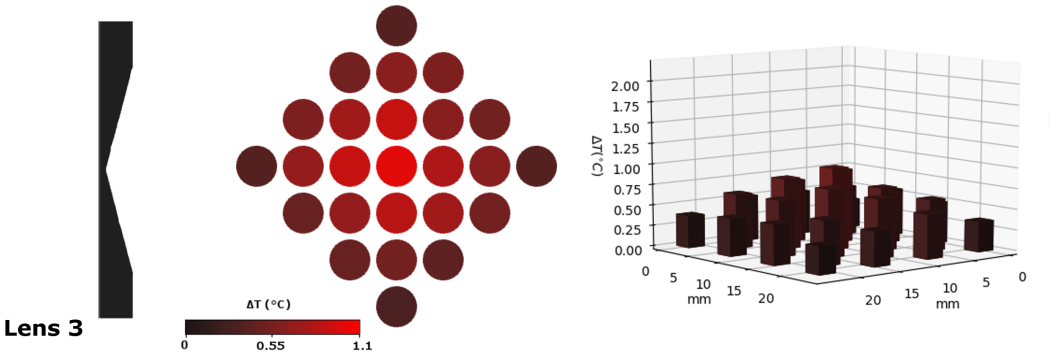

Figure 23: Results for Lens 3, with the sensor positioned 7.5 cm from the lens.

Lens 3 was designed to diverge the beam uniformly to avoid introducing diffraction effects caused by varying the deviation angle of the beam. Also, the incident surface was made planar to minimize surface reflection.

The resulting irradiance is more uniform than through the 2.5-mm disk, but at the cost of considerable loss at the location of the sensor. An examination of the irradiance curve of the center row of pixels suggests that some of this loss is due to the beam being refracted

beyond the area of the sensor, where the irradiance through the lens is higher than through the disk.

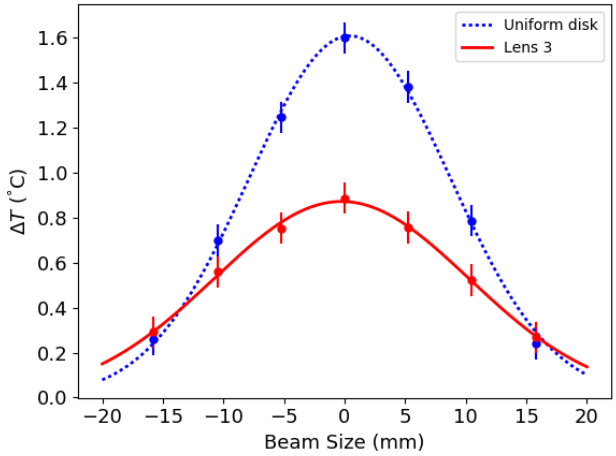

Figure 24: The irradiance through Lens 3 is more uniform than through the 2.5-mm disk but at the cost of considerable loss.

5.3.4 Lens 4 (Thin Lens)

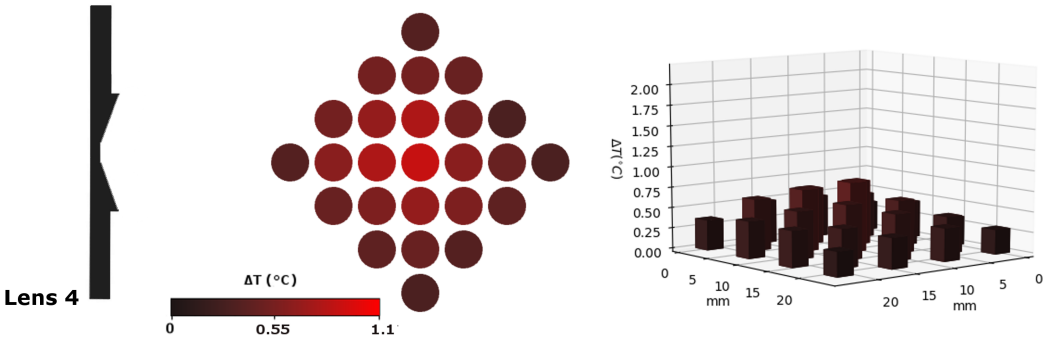

Figure 25: Results for Lens 4, with the sensor positioned 7.5 cm from the lens.

This lens was designed to minimize absorption losses and diverge only the central hot spot of the beam. The results show considerable irradiance loss across the full profile, despite the lens being thinner than the 2.5-mm disk at most points. Total internal reflection of the beam can be ruled out by noting that the angle of incidence at the second lens face, 20° (see Fig. 31 in Appendix B), is far from the critical angle for a refractive index of 1.46 (∼43.23°).

A close examination of the heat map in Fig. 25 suggests that some of this loss is due to the lens being misaligned, as the refracted beam is slightly off-center and the sensor is not capturing the full irradiance profile.

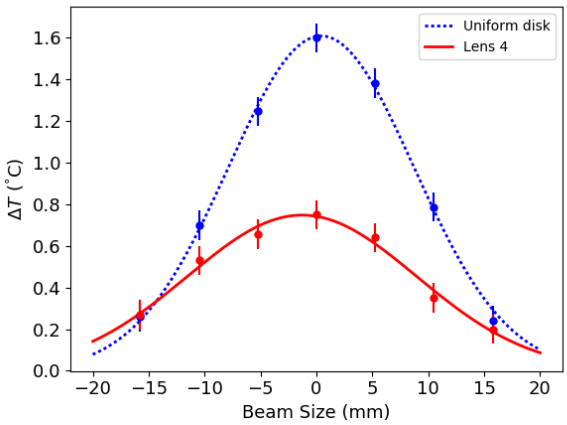

Figure 26: The irradiance through Lens 4 along the center row of pixels shows a slightly misaligned beam, accounting for some of the loss across the sensor.

5.3.5 Lens 5 (Thick Conic Lens)

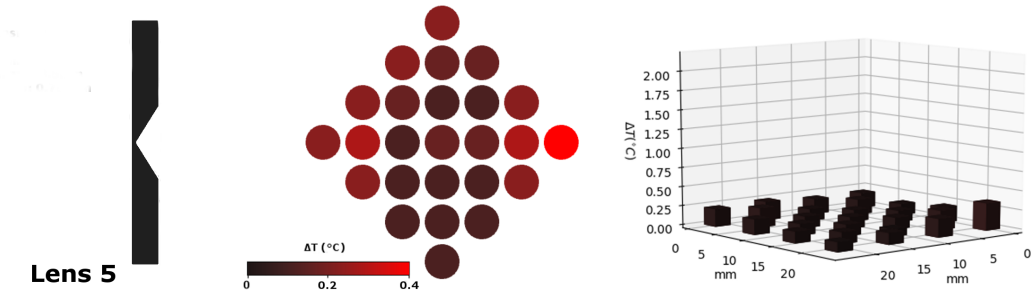

Figure 27: Results for Lens 5, with the sensor positioned 7.5 cm from the lens. Note the small temperature range of the heat map.

Almost all of the irradiance is lost at the center of the beam profile, with a slight increase in irradiance along the perimeter. The angle of incidence at the second lens face is 32°, so total internal reflection of the beam is unlikely.

A second measurement with the sensor positioned closer to the lens (4 cm) suggests that the loss seen in Fig. 27 is largely due to the beam being refracted beyond the area of the sensor. At 4 cm from the lens, the beam irradiance along the perimeter of the sensor is higher than even the unobstructed beam.

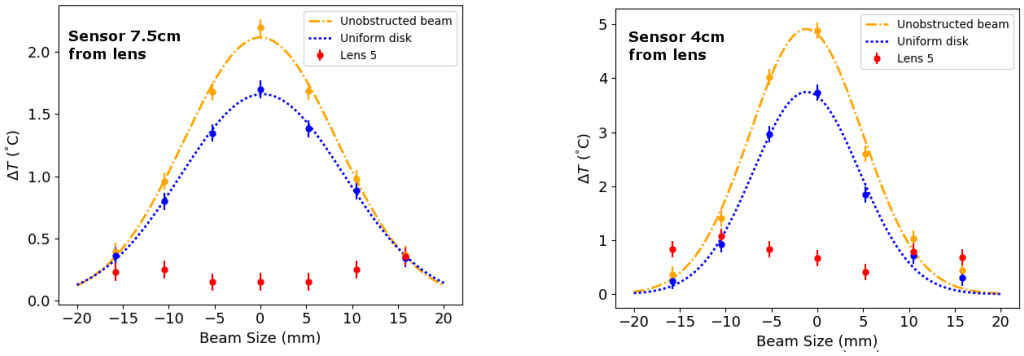

Figure 28: A comparison of the performance of Lens 5 at two different locations along the beam path indicates that the lens is refracting the beam beyond the solid angle of the sensor. At 4 cm from the lens, the irradiance on the outer sensor pixels is higher with the lens in place than the unobstructed beam.

These results suggest that a lens of this design might work to evenly saturate a DNP target with minimal loss if the angle of the lens were modified such that the refracted beam were kept within the area of the target. However, as with most of the lenses in this study, a slight misalignment of the lens completely alters the resulting irradiance pattern. Lens alignment is a major challenge that will need to be overcome before such lenses can be implemented into a DNP system.

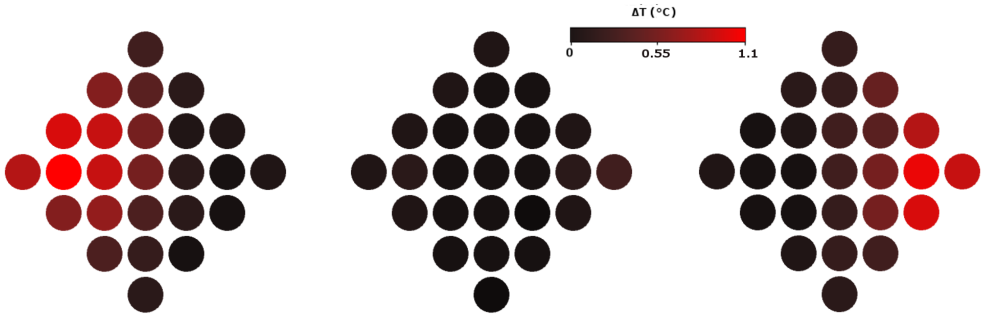

Figure 29: A slight adjustment to lens alignment can have a dramatic effect on the direction of the refracted beam. If not precisely centered, Lens 5 functions as a prism, refracting the beam to one side of the sensor.

5.4 NMR of 3D-Printed Kel-F

To conclude the study of the properties of 3D-printed Kel-F relevant to its use in DNP, a brief proton NMR analysis was performed on a sample of heavily processed Kel-F. As mentioned in the Background and Motivation section, Kel-F is favorable because it contains no free protons that could introduce a background into the NMR signal used to measure the polarization of the target. The question of whether the 3D-printing process was introducing hydrogen into the material was thus of interest.

The measurements were made using a Teltron NMR/ESR module [30] used in the senior laboratory class taught at the University of New Hampshire. The data were captured using a Rigol DS1102E oscilloscope. The results are given in Fig. 30, along with results obtained from a sample of Durable resin, the material used for the target ladder in Fig. 16.

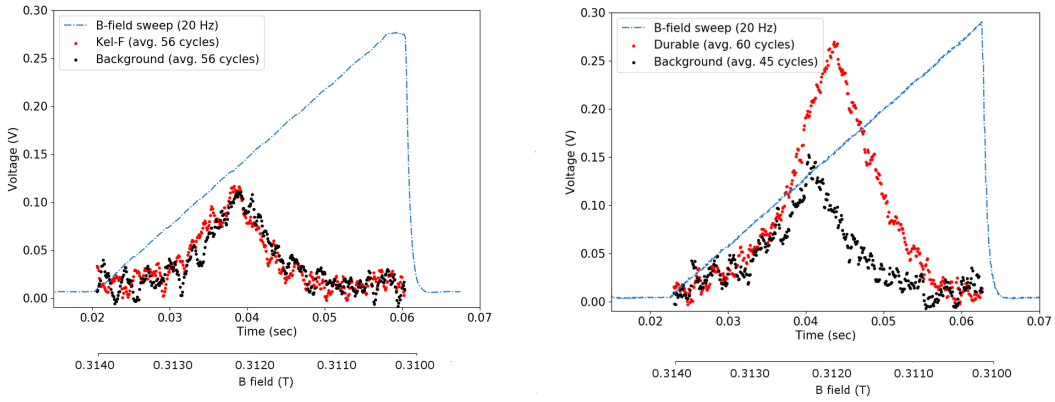

Figure 30: Proton NMR analysis of a sample of heavily processed Kel-F showed no indication of hydrogen content when plotted with the background signal from the probe (frequency 13.15 MHz). A similar measurement on Durable resin yielded a significant proton NMR signal compared to the background (13.17 MHz probe frequency). The sensitivity of the probe was higher for the Durable measurement, accounting for the larger background peak in that plot.

6 Summary and Conclusions

The results of this paper show that DNP target cups can be successfully 3D printed using Kel-F. These cups have the same favorable properties as solid, machined Kel-F, namely, plasticity at cryogenic temperatures, transparency to mm-waves, and the absence of a proton NMR signal. Measurements of the transparency of Kel-F to 140 GHz radiation, however, revealed that some loss occurs due to surface reflection and absorption of both solid and 3D-printed Kel-F, although less than for Formlabs Durable resin.

These reflection and absorption losses place limits on the design of mm-wave Kel-F lenses if they are to be implemented into a DNP target system to enhance nucleon polarization. Of the five lenses tested in this study, all five resulted in significant mm-wave loss at the location of the sensor. Further analysis is necessary to determine whether this is primarily due to mm-wave transmission loss through the lenses or whether the lenses are simply spreading

the beam beyond the solid angle of the sensor. A clear next step will be to make more measurements with the sensor positioned at various locations along the beam path, as was done with Lenses 1 and 5 in this study.

To improve lens performance, future lenses might be designed with the use of optical software to model the expected behavior of the lenses, including diffraction effects, which were a major area of uncertainty in this study.

A greater challenge perhaps than loss of irradiance is lens alignment. To achieve a uniform irradiance profile, most of the lenses featured in this study had to be very precisely centered on the mm-wave beam. This presents a considerable technical challenge if such lenses are to be used to evenly saturate a nucleon target in a DNP system. On the other hand, this appears to be less of an issue for lenses with shallower angles of incidence (Lens 3 in this study), and improvements to lens design might help resolve this problem.

Appendices

Appendix A

Table 2: Settings for Kel-F filament production using the Filatizer.

Die (mm)	Temp. (°C)	Speed (cm/min)	Filament (mm)	Notes:
2	360	13	1.75±0.1	No cooling fan.
1.65	380	17	1.7±0.1	Cooling fan on filament.

Table 3: Settings for Kel-F and FEP printing on a modified Prusa i3 MK2.5S printer using Slic3r software to generate gcode.

	Kel-F		FEP
Filament (mm)	1.75±0.1	1.7±0.1	1.80±0.05
Fill density (%)	100	100	20
Flow rate (%)	80	70-80	100
Layer height (mm)	0.2	0.1	0.2
First layer:			
Temp. (°C)			
Nozzle	360	370	410
Bed	115	unheated	100
Speed (mm/sec)	6	7.5	1.5
Extrusion width (mm)	0.42	0.42	0.42
Subsequent layers:			
Temp. (°C)			
Nozzle	360	370	420
Bed	115	unheated	100
Speed (mm/sec)			
Perimeter	7.5	15	4.5
Small perimeters	3	6	1.8
External perimeters	6	12	3.6
Infill	9	18	5.4
Solid infill 7.5	15	15	4.5
Top solid infill 8	16	12	3.6
Gap fill	4.5	9	3.6
Extrusion width	0.45	0.45	0.45
Print fan	Off	Off	Off
Notes:	Printed atop acrylic adhesive		Printed atop FEP tape

Appendix B

Equations for a lens surface that creates a plane wave from an incident Gaussian beam, obtained from [29]:

$$r^2 = \omega_0^2(\hat{z}_p + \hat{z}_p^{-1})(\Gamma + \arctan(\hat{z}_p) - \arctan(\hat{z}_0)) \tag{7}$$

$$\hat{z}_p = \frac{2z_p}{k\omega_0^2}, \qquad \hat{z}_0 = \frac{2z_0}{k\omega_0^2} \tag{8}$$

$$\Gamma = \frac{1}{2}(n-1)k^2 w_0^2(\hat{z}_p - \hat{z}_0) \tag{9}$$

Here w_0 is the beam waist, k is the beam wave number, z_0 is the distance from the beam waist to the lens face, and n is the refractive index of the lens material.

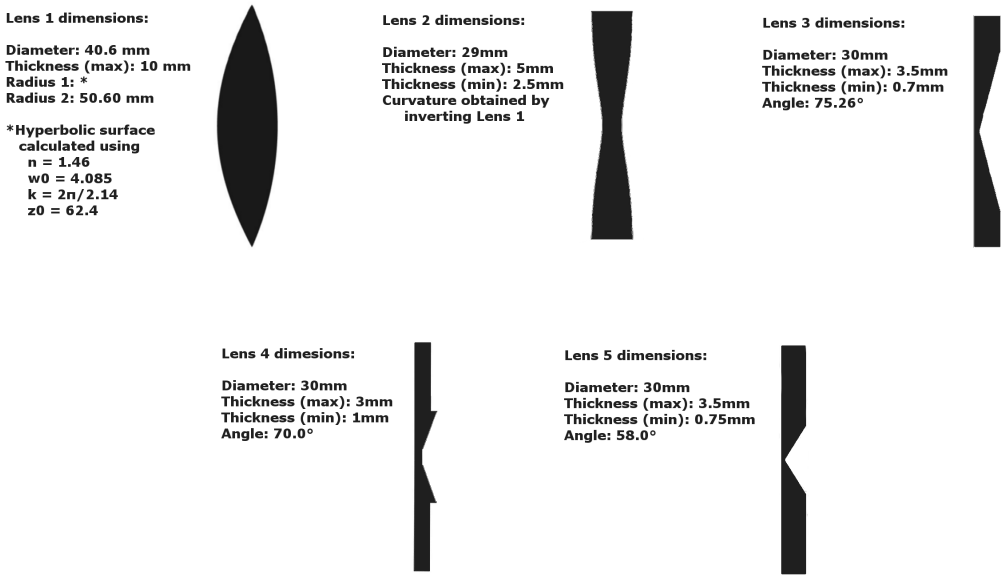

Figure 31: Dimensions for 3D-printed Kel-F lenses.

References

[1] K. Slifer, et al, JLab PAC40, C12-13-011 (2013).

[2] P. Hoodbhoy, et al, Nucl. Phys. B 312, 571 (1989).

[3] L. Frankfurt, M. Strikman, Phys. Rept. 160, 235 (1988).

[4] E. Long, et al, Jefferson Lab Proposal C12-15-005 (2016).

[5] W. Meyer, et al., Nucl. Instr. Meth. A 244, 574 (1986).

[6] D.G. Crabb, W. Meyer, Annu. Rev. Nucl. Part. Sci. 47, 67 (1997).

[7] J. Pierce, et al. Nucl., Instr. Meth. A 738, 54-60 (2014).

[8] X. Wang, et al, Application of Additive Manufacturing in the Development of a Sample Holder for a Fixed Target Vector Scanning Diffractometer at SwissFEL.

[9] A. R. Phipps, et al, Nucl. Instrum. Meth. B 402, 202 (2017).

[10] Kutz, M. Applied Plastics Engineering Handbook: Processing and Materials. 1st Ed. (2011).

[11] Ebnesajjad, S. Fluoroplastics Volume 2: Melt Processible Fluoropolymers - The Definitive Users Guide and Data Book. 2nd Ed. (2015).

[12] pro-K Fluoropolymergroup, Product information Polychlorotrifluoroethylene (PCTFE), accessed 5/10/2019 at http://www.pro-kunststoff.de/wp-content/uploads/2015/02/TM-7-Polychlorotrifluoroethylene_PCTFE.pdf.

[13] United State EPA 822-F-18-001, 2018 Edition of the Drinking Water Standards and Health Advisories Tables, accessed 5/12/2019 at https://www.epa.gov/sites/production/files/2018-03/documents/dwtable2018.pdf.

[14] Ebnesajjad, S. Fluoroplastics Volume 1: Non-Melt Processible Fluoropolymers - The Definitive Users Guide and Data Book. 2nd Ed. (2015).

[15] Professional Plastics, Typical Properties of Kel-F/PCTFE, accessed 5/10/2019 at https://www.professionalplastics.com/professionalplastics/content/downloads/Kel-FData.pdf.

[16] Filastruder filament production system available at https://www.filastruder.com.

[17] PCTFE and FEP bulk material purchased from Professional Plastics. https://www.professionalplastics.com.

[18] Professional Plastics, Typical Properties of Selected Fluoropolymers, accessed 5/10/2019 at www.professionalplastics.com/professionalplastics/content/PTFE_FEP_PFA.pdf.

[19] Prusa i3 MK2.5S 3D-printer available at https://www.prusa3d.com.

[20] Nickle-plated 3D-printer heater block obtained from E3D-Online. https://e3d-online.com/v6-plated-copper-heater-block.

[21] Silicon adhesive transfer tape (Product No. 7615A41) obtained from McMaster-Carr. https://www.mcmaster.com/7615a41.

[22] Thorsten Maly. Private communication.

[23] Pedrotti, F.L., Pedrotti, L.M., Pedrotti, L.S. Introduction to Optics. 3rd Ed. Cambridge University Press. p 587. (2017).

[24] S. Ohkoshi, et al, A MillimeterWave Absorber Based on GalliumSubstituted Iron Oxide Nanomagnets. Angewandte Chemie International Edition, 46 (2007).

[25] Temperature-sensitive liquid crystal sheets obtained from Edmund Optics. www.edmundoptics.com/p/35-36deg-c-temp-range-liquid-crystal-sheet-/24206/.

[26] Keysight Technologies. Basics of Measuring the Dielectric Properties of Materials, Application Note, literature number 5989-2589EN.

[27] A.H. Scott, et al, Journal of Research of the National Bureau of Standards–A. Physics and Chemistry Vol. 66A, No. 4 (1962).

[28] Goldsmith, P.F. Quasioptical Systems: Gaussian Beam Quasioptical Propagation and Applications. IEEE Press. p 1. (1998).

[29] Lesurf, J.C.G. Millimetre-Wave Optics, Devices and Systems. 18. (1990).

[30] Teltron NMR manual available at https://www.a3bs.com/esrnmr-basic-set-115-v-5060-hz-1000637-u188031-115-3b-scientific-teltron,p_667_16637.html.